

Wind influence on surface current variability in the Ibiza Channel from HF Radar

Arancha Lana¹ · Julien Marmain² · Vicente Fernández³ · Joaquin Tintoré^{1,2} · Alejandro Orfila¹

Received: 6 October 2015 / Accepted: 25 January 2016 / Published online: 4 March 2016
© Springer-Verlag Berlin Heidelberg 2016

Abstract Surface current variability is investigated using 2.5 years of continuous velocity measurements from an high frequency radar (HFR) located in the Ibiza Channel (Western Mediterranean Sea). The Ibiza Channel is identified as a key geographical feature for the exchange of water masses but still poorly documented. Operational, quality controlled, HFR derived velocities are provided by the Balearic Islands Coastal Observing and Forecasting System (SOCIB). They are assessed by performing statistical comparisons with current-meter, ADCP, and surface lagrangian drifters. HFR system does not show significant bias, and its accuracy is in accordance with previous studies performed in other areas. The main surface circulation patterns are deduced from an EOF analysis. The first three modes represent almost 70 % of the total variability. A cross-correlation analysis between zonal and meridional wind components and the temporal amplitudes of the first three modes reveal that the first two modes are mainly driven by local winds, with immediate effects of wind forcing and veering following Ekman effect. The first mode (37 % of total variability) is the response of meridional wind while the second mode (24 % of total variability) is linked primarily with zonal winds.

The third and higher order modes are related to mesoscale circulation features. HFR derived surface transport presents a markedly seasonal variability being mostly southwards. Its comparison with Ekman-induced transport shows that wind contribution to the total surface transport is on average around 65 %.

Keywords Surface currents · HF Radar · Mass transport · Wind-current variability · Ibiza Channel · Mediterranean sea

1 Introduction

The study of mass transport at the sea surface is of great interest for many ecological, environmental, and engineering applications such as the advection of larvae, oil spills, or search and rescue operations among others. The transport and fate of pollutants as well as the dynamics of particulate material at the upper ocean layer are key elements in coastal and open ocean studies at multiple temporal scale (Pinardi et al. 2003; Sayol et al. 2014; Liu et al. 2014).

In the Western Mediterranean Sea (WM), several areas have been identified as extremely relevant for the exchange of water masses, e.g., the Alboran Sea, the Almeria-Oran Front, the Gulf of Lions, the Sicily, and the Ibiza Channels (Millot 1999).

The Ibiza Channel is a key geographical feature connecting two different sub-basins, the Northwestern Mediterranean and the Alboran Sea, therefore, controlling the passage of water masses with very different origin (Lopez-Garcia et al. 1994; Mason and Pascual 2013). Its relative interest in the Mediterranean circulation lies not only on the study of the dynamical properties derived from the intense frontogenetic activity occurring there but also

Responsible Editor: Birgit Andrea Klein

✉ Julien Marmain
jmarmain@socib.es

Alejandro Orfila
aorfila@imedea.uib-csic.es

¹ IMEDEA (CSIC-UIB), 07190 Esporles, Spain

² ICTS-SOCIB, 07121 Palma de Mallorca, Spain

³ EUROGOOS AISBL, 1050 Brussels, Belgium

because there is a periodic input of nutrients advected from recent Atlantic Waters (rAW) coming from the Strait of Gibraltar (Zavatarelli and Mellor 1995; Viudez et al. 1996; Juza et al. 2013; Sayol et al. 2013). The highly temporal and spatial variability of water transport in this area requires continuous measurement of its dynamics by means of a routinely monitoring strategy.

Besides, the study of the Ibiza Channel is specially challenging due to the wide temporal and spatial scales of the oceanic processes occurring there. A description of the surface circulation in this region has been already performed by synoptic observations from oceanographic cruises (Pinot et al. 2002), satellite observations (Troupin et al. 2015), and numerical models (Renault et al. 2012; Juza et al. 2013), as well as with gliders (Heslop et al. 2012). All these works are centered to study specific processes in a reduced period of time or to a reduced area. The influence of the wind-induced variability versus internal variability remains an open question.

During the last years, the need of continuously monitoring the coastal ocean in order to improve the reacting capacity of the operational systems has been identified. Indeed, the marine strategy from the European Commission indicates as a priority the establishment of Coastal Observing System (COS) in order to provide quality data in near real-time (Orfila et al. 2015), especially important at coastal areas. New monitoring technology has been progressively implemented in coastal multi-platform ocean observatories. The high frequency radar (HFR) technology allows the real-time measuring providing a new, detailed, and quantitative description of physical processes at the marine surface (Paduan and Washburn 2013). The wide-world expansion of HFR observing facilities is setting new standards of the coastal observing capabilities. The HFR network used for operational purposes is well established at both US coasts (Harlan et al. 2010) and is also increasing in the European context (Bellomo et al. 2015).

Since 2012, a continuous monitoring of surface circulation in the Ibiza Channel is performed, thanks to the installation of two HFR coastal stations, as part of the Balearic Islands Coastal Observing and Forecasting System (SOCIB) ocean observing facilities (Tintore et al. 2013). This HFR provides operational surface currents at the eastern side of the Ibiza Channel (up to 70 km from the coast of Ibiza) allowing for the first time a synoptic view of the coastal surface currents during a large period of time.

Additionally, an oceanographic moored buoy, equipped with a weather station, a surface current-meter and an Acoustic Doppler Current Profiler (ADCP), deployed inside the HFR coverage, provides point wise subsurface currents data. Wind observations acquired at the weather station installed on the oceanic buoy can be used to estimate the wind-induced transport.

In this paper, we analyze the surface circulation in this area using 2.5 years of velocity data from HFR focusing on the variability of the surface transport induced by wind. The paper is structured as follows. In Section 2, the study area as well as the data used and the methodology are described. In this section, we also present the quality of the HFR velocities which is tested against data from ADCP, current-meter, and Lagrangian drifters. In Section 3, the most relevant circulation patterns are explained from the wind variability and the induced surface transport quantified. Finally, Section 4 concludes the work.

2 Data and methods

2.1 HFR data in the Ibiza Channel

The Ibiza Channel is defined as the section crossing zonally the WM between the Iberian Peninsula and the Ibiza and Formentera islands (white box, Fig. 1a). It comprises the area bounded by transects $38^{\circ} 11' N$ and $39^{\circ} 11' N$ of latitude and between Cape la Nao located at $0^{\circ} 10' E$ and the coast of Ibiza Island at $1^{\circ} 12' E$. This channel has a width of ~ 80 km and a sharp bathymetry with a depth reaching 1000 m in the central part.

The Ibiza Channel is a key area for the dynamics of the whole WM basin where the northern current (NC) flowing southwards encounters and interacts with the northward flow of the rAW impulsed by energetic Alboran and Algerian basin mesoscale structures (see Fig. 1a for the sketch of the main circulation features around the Balearic islands). On the other hand, both southward and northward flows bump into the sharp bathymetric change generating frequent mesoscale structures that contribute to the destabilization of both fronts (Pinot et al. 1994; Pinot and Ganachaud 1999; Ruiz et al. 2009; Heslop et al. 2012).

The interest in the study of the surface circulation in the Ibiza Channel increased in the last two decades thanks in part to the establishment of a program of continuous observation mainly from oceanographic cruises (Lopez-Jurado et al. 1995; Pinot et al. 1994). The satellite observations (Mason and Pascual 2013) and numerical models (Renault et al. 2012; Juza et al. 2013) have also contributed in the knowledge of the variability of the surface circulation in the area.

In the last years, the implementation of a continuous multiplatform observation system increased the quantity and quality of available data (Tintore et al. 2013). In particular, the HFR provides high-resolution synoptic observation of the surface currents. The monitoring system is based on two monostatic medium-range Coastal Ocean Dynamics Applications Radar (CODAR) SeaSonde system (Paduan and Rosenfeld 1996) operated by SOCIB (Lana et al. 2015).

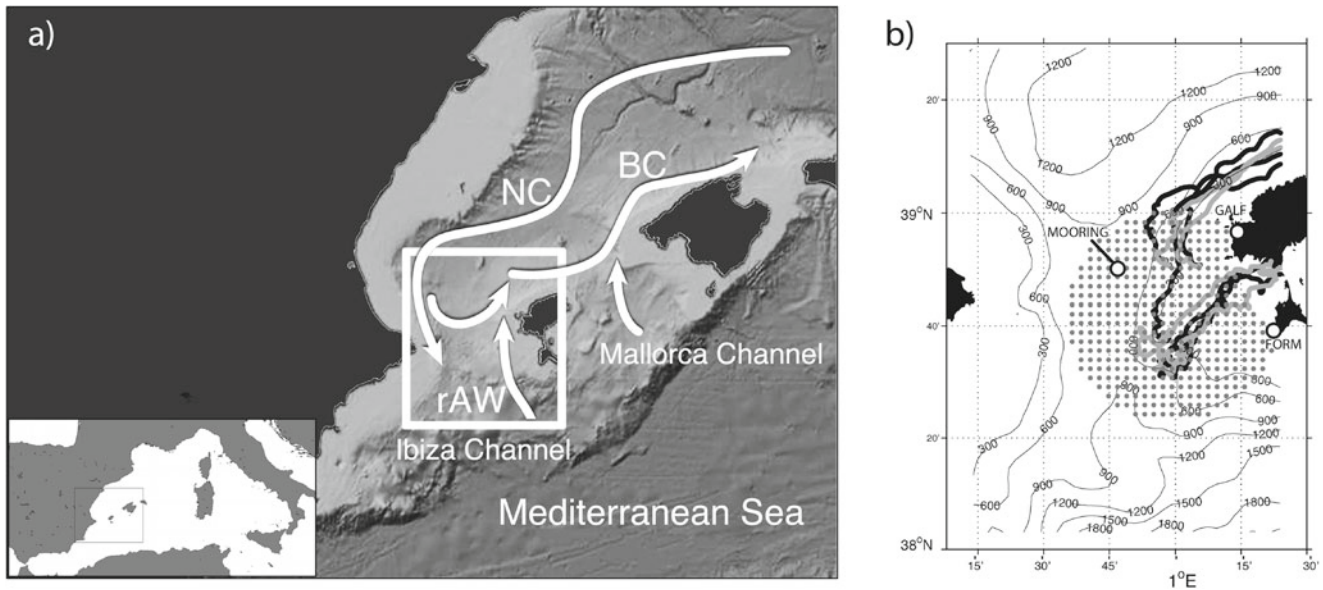


Fig. 1 **a** Location of the area of study in the Western Mediterranean sea (WM). The *white box* sketches the Ibiza Channel and *white arrows* depict the main oceanic circulation pathways around the Balearic Islands. **b** Ibiza Channel bathymetry (in meter) and location of observations used in this study. The Ibiza (GALF) and Formentera (FORM) HFR stations are sketched by *big white point*. *Small black points* show the HFR derived surface current total vector grid. The *big white point*

in the HFR coverage indicates the position of the Ibiza Channel mooring where ADCP and Current Meter are set. Meteorological stations, providing wind information, are also present at GALF and on the Ibiza Channel mooring. Drifter trajectories (CODE and MDi) from the Ibiza Channel Validation Experiment are shown in *black* and *grey*, respectively

The first station is located on the western coast of Ibiza island (hereinafter GALF) and the second one on the western coast of Formentera island (hereinafter FORM) (see Fig. 1b). This shore-based remote-sensed technique relies on the Bragg resonance phenomenon. Each HFR station emits with a central frequency of 13.5 MHz and a bandwidth of 90 kHz, reaching ranges up to 70 km. Emitted electromagnetic waves are back-scattered by oceanic surface gravity waves of exactly half the HFR wavelength (Crombie 1955). Radial velocities (velocities toward or away from the antenna) are derived from the Doppler shift due to the difference between ideal and measured Bragg frequency (Barrick et al. 1977). Despite the exact depth of HFR velocity measurement is still under active discussion in the HFR community, it is generally assumed that it depends on the working frequency of the HFR and corresponds to a vertical weighted average of the horizontal velocity. For this HFR frequency, the velocities correspond to an average on the first 0.9 m (Stewart and Joy 1974; Laws 2001).

The radial velocity maps for each antenna are produced on a grid with an azimuthal discretization of 5° and a nominal radial resolution of 1.6 km. Radial velocities are derived using the classical CODAR processing (Paduan and Rosenfeld 1996), i.e., the velocities are processed from an averaged spectra of 15 min of the received echoes every 10 min and finally the hourly radial velocities obtained after applying a 75 min running average. Integration is performed

roughly every hour with the Multiple Signal Characterization (MUSIC) algorithm (Schmidt 1986). Hourly radial velocity maps from both stations are combined to produce the cartesian velocities on a regular 3 × 3 km grid, using an unweighted least square method applied locally within a 6-km radius around each grid point (Lipa and Barrick 1983; Shay et al. 2007). Geometric dilution of precision (GDOP) results in a global accuracy around ±4 cm/s in the worst cases (Chapman et al. 1997). A mask is applied to prevent large error due to GDOP, typically due to angles between radial direction <30° or >150°. The final velocities are provided on 393 grid points over an area covering 0° 36′–1° 21′ E and 38° 24′ and 38° 59′ N (Fig. 1b).

An automatized post-processing quality control test is applied to the velocities in order to detect spikes (instantaneous and first time derivative) (Roarty et al. 2012). Valid range for velocity with a 70 cm/s threshold is also checked (Lana et al. 2015). The HFR data quality control (QC) relies on state-of-the-art QC procedures applied both on radial and total velocities. CODAR standard QC procedures are applied prior an operational battery of tests. Both antennas have been calibrated measuring their patterns following the standard procedure of the Seasonde radar.

For the present study, we use real-time hourly data for the period from June 1st 2012 to January 22nd 2015 (data can be downloaded from www.socib.es). The total velocities can contain gaps both in time and space due to system failures

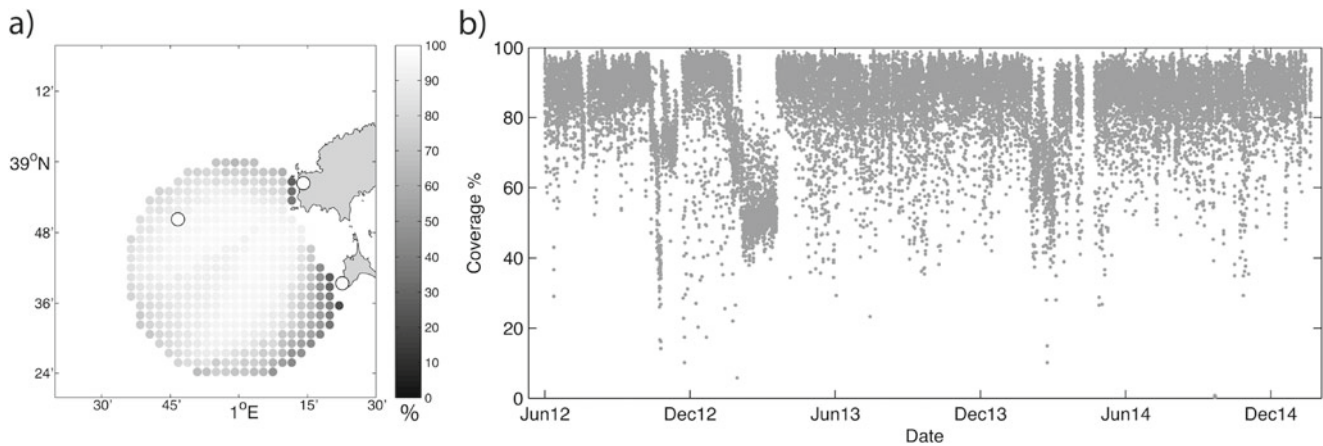


Fig. 2 **a** Spatial distribution of the temporal coverage and **b** temporal variation of the spatial coverage of HFR total velocities between June 2012 and January 2015. A spatial coverage of 100 % is when the

maximum number of grid nodes with total velocities (393 nodes). Mooring and HFR station locations are also shown

or signal processing that induce missing radial velocities. Figure 2a shows the percentage of measured data for each of the 393 spatial points. The range of available data is between 95 % at the central part of the domain to a 10 % in the south-eastern part where the signal from the GALF antenna is frequently interfered. For this period, near 70 % of the time, the spatial coverage is larger than the 80 % of the points (Figure 2b) but, as seen in some dates, there is no data (5 % of the time) due to multiple causes (specifically strong storms that caused failures at the stations, during January 2013 and February 2014, and hardware damage during November 2012).

2.2 Current-meter, ADCP, lagrangian drifters, and wind data

In 2013, an oceanographic buoy was moored within the HFR coverage area. The buoy is located at $38^{\circ} 49.46' N$ and $0^{\circ} 47.02' W$ (Fig. 1b). Currents are measured by a current-meter (CM) deployed at 1.5-m depth. The instrument is a two-dimensional Falmouth Scientific Inc. acoustic CM (2D-ACM) integrated in a fixed platform, which use the phase-shift acoustic transit-time measurement technique. Additionally, at 1-m depth, a downward-looking SONTEK

ADCP water profiler measures the current between 5- and 125-m depth (250-kHz) every 5 m. Velocities from CM and from the upper ADCP layer (at 5 m depth) are used for comparison with the HFR surface current data. Both ADCP and CM current measurements are integrated over 3 min and provided every hour in real time. The quality controlled data flagged as good or probably good (following European Directive INSPIRE, European Commission 2007) are used. Data can be downloaded at <http://thredds.socib.es/thredds/catalog.html>.

Because of maintenance, the mooring was taken out for some months. Taking into account the availability of CM (respectively, ADCP) data, period 1 (respectively, period 2) is used for comparison with HFR data (Fig. 3). Despite the different technologies used as well as the different measurement depths, the comparison provides a comprehensive validation of HFR over time.

The spatial accuracy of the HFR is assessed in the Lagrangian framework using 13 surface drifters. The drifters used are MetOcean CODE oceanographic surface drifters with drogues between 30 and 100 cm, long life battery and low wind-exposure; MD03i which has surface current tracker, flexible, and rigid drogues and low wind-exposure and ODI drifter with a small ~ 5 kg weight drogue

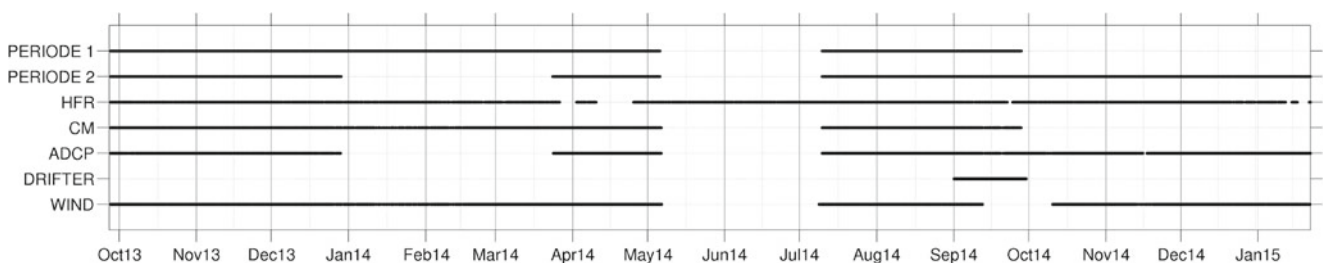


Fig. 3 Temporal availability of each observing system and definition of periods used to validate the HFR velocities

and high wind exposure. Three different kinds of drifters were launched at four different positions during a validation exercise performed in September 2014 (see drifter tracks at Fig. 1b).

Wind speed and wind direction were measured every 10 min at two meteorological stations located at the buoy and at GALF station (Fig. 1b). The wind rose for September 2013 to January 2015 is represented using a 3 h average in Fig. 4. Winds blowing from south-west and from west-north-west directions prevail influenced by the continental topography. Wind speed rarely exceed 14 m/s in this area.

2.3 HFR validation

Assessment of operational HFR total velocities is performed both in the Eulerian framework, by comparing the velocities from HFR with those from the CM and the ADCP, and also in a Lagrangian framework by comparing against surface drifter derived velocities. The nearest grid point is ~1400 m away from the mooring location and it is selected for the Eulerian comparison. For the lagrangian comparison, drifter velocities have been averaged over 75-min periods centered at each round hour whereas comparisons are hourly performed for both (U and V) drifter velocity data against all available HFR data within a distance of 1500 m of the drifter.

The comparison between these data is not straightforward since they measure velocities at different temporal and spatial scales (Rubio et al. 2011; Forget 2015). The power

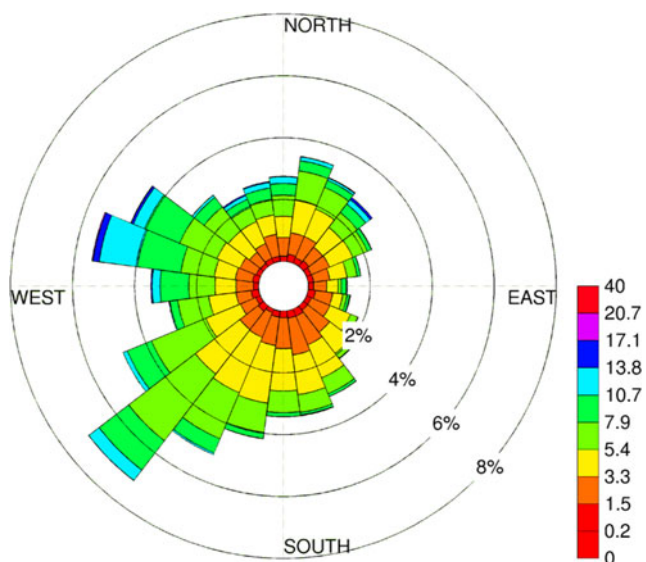


Fig. 4 Wind rose (occurrence of wind speed per direction sector) from September 2013 to January 2015. Wind speed color bar is given following the Beaufort scale (from calm to near gale and above near gale) in m s^{-1} . Wind speed and direction are derived from the 75-min averaged zonal and meridional wind components. Wind direction follows the meteorological convention

spectra of the CM velocities (black line) and of the nearest HFR location (gray line) are given in Fig. 5. Spectra were computed using the Welch method with an averaged periodogram of overlapped windowed signal sections with a 95 % of confidence. As seen, both signals present the same dominant peaks located at the diurnal (~24 h) and inertial (~19 h) frequencies. According to the tidal representation using the HFR in the area (not shown), the principal lunar semidiurnal tidal (M2) is clearly related with the bathymetry distribution. Along the basin direction, there are reversing tidal currents, mainly with southern direction, with intense amplitude over the coastal platform (~3.5 km) decreasing offshore. The plateau observed in the high frequency part of HFR spectra and, to a lesser extent, of CM current spectra reflect intrinsic noise properties as reported by

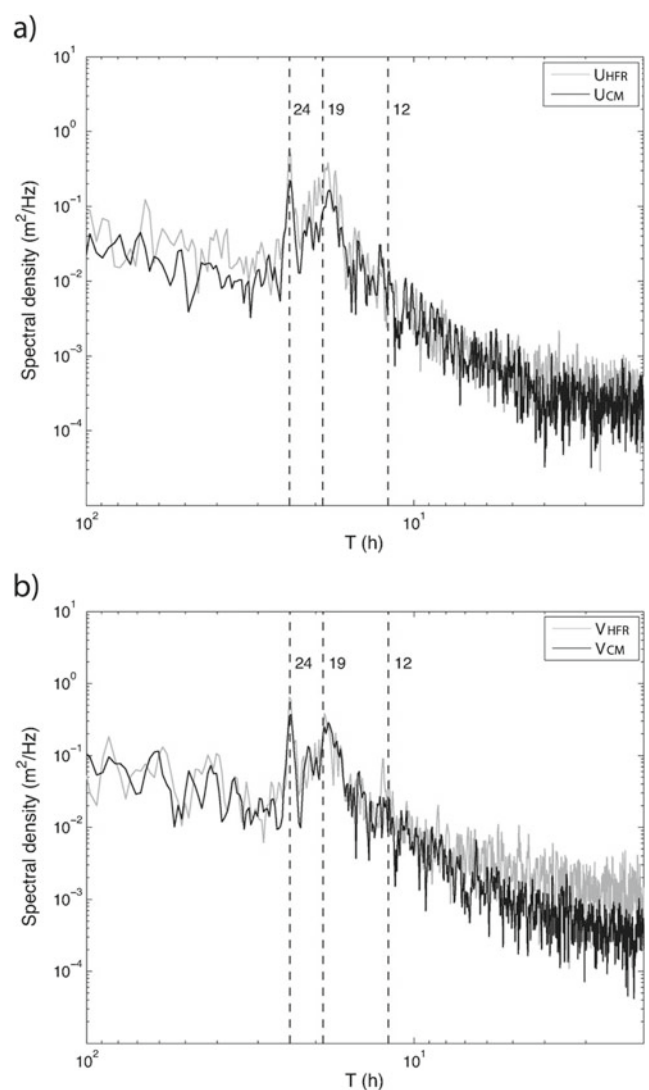


Fig. 5 Power spectra of normalized V component inferred from: HFR data at the nearest grid to the mooring position (grey) and for the mooring current meter V component (black) for the period Sept 2013–Sept 2014

Table 1 Statistical comparison between 6-h averaged HFR and CM or ADCP zonal (u) and meridional (v) velocities

	N	RMS_X		RMS_{HFR}		STD_X		STD_{HFR}		$RMSD$		$BIAS$		CC	
		u	v	u	v	u	v	u	v	u	v	u	v	u	v
CM vs HFR	960	11.0	11.8	10.2	14.9	10.6	11.6	9.9	13.9	7.7	12.0	-0.6	-2.7	0.72	0.59
ADCP vs HFR	1092	9.3	13.9	8.9	14.3	9.2	11.6	8.7	12.0	7.3	10.2	0.1	-0.1	0.67	0.63

Comparison between HFR and CM (respectively ADCP) is performed over period 1 (respectively period 2) defined in the main text. The root mean square (RMS) and standard deviation (STD) are given for each component of the compared data. X stands for CM or ADCP. The RMS difference (RMSD), bias (BIAS), and correlation coefficient (CC) are computed. N is the total number of data used for comparisons. RMS, STD, RMSD, and BIAS are in cm/s

Forget (2015). This noise effect results in an effective minimum period of the geophysical signal that can be extracted greater than the 2-h Nyquist period (typically 6 h). Following this ascertainment, HFR, CM, and ADCP velocities are 6-h averaged to compute the Eulerian comparison. Note the differences in power and the fact that both instruments have dominant peaks at near inertial (~ 19 h) and diurnal tidal frequencies (~ 24 h)

Values for the comparison among the different velocities are given in Table 1 where the statistical parameters are given in Appendix. For all instruments, root mean square (RMS) and standard deviation (STD) of V-component are higher than for U-component, indicating that surface currents are more variable and, in average, mainly oriented in the meridional direction in the central part of the Ibiza Channel. RMSD computed between HFR and either CM or ADCP do not sketch significant differences. However,

the V-component RMSD is higher than the U-component RMSD due to the higher variability of surface currents in the meridional direction and to the GDOP effect which ends in higher errors in the V-component during the combination of radial velocities. Following this comment, note that HFR radial geometry at the mooring location let the GALF radial direction almost colinear to the zonal direction. These explain why the correlation coefficient (CC) of U-component is higher than the CC of V-component. The main result is that HFR total velocities do not sketch significant errors, in agreement with similar studies (Cosoli et al. 2010; Emery et al. 2004; Lorente et al. 2014; Rubio et al. 2011). Statistical figures between drifters and the HFR velocities are given in Table 2. The values of CC and RMSD indicate a good agreement between both measurements and are also in accordance with previous studies (Paduan et al. 2006; Lorente et al. 2014; Solabarrieta et al. 2014).

Table 2 Statistical comparison, performed over September 2014, between hourly HFR and drifter (*dri*) derived zonal (U-component) and meridional (V-component) velocities

Drifter	N	U-component				V-component			
		RMS_{dri}	RMS_{HFR}	$RMSD$	CC	RMS_{dri}	RMS_{HFR}	$RMSD$	CC
ODI017	116	10.67	6.52	6.45	0.82	16.34	9.48	10.79	0.77
ODI018	119	9.82	6.42	5.64	0.84	16.24	9.21	10.79	0.77
ODI004	122	14.22	9.09	9.51	0.73	21.40	10.93	19.08	0.48
ODI006	135	12.22	9.49	9.60	0.65	13.12	11.34	8.25	0.79
MDI001	28	6.58	6.76	4.85	0.73	12.09	9.18	11.47	0.73
MDI002	93	4.71	6.84	5.01	0.65	6.25	6.12	7.34	0.27
MDI003	113	6.25	6.77	3.87	0.86	11.74	10.53	7.23	0.87
MDI004	173	8.57	9.38	5.92	0.78	10.67	11.45	6.88	0.81
MDI004r	176	9.26	9.57	5.56	0.83	10.81	11.23	6.77	0.83
CODE001	69	6.87	6.86	5.76	0.58	8.02	8.61	7.62	0.44
CODE002	58	8.23	6.38	7.07	0.80	7.22	7.49	6.31	0.45
CODE003	148	9.00	8.50	3.79	0.90	9.71	10.28	5.68	0.87
CODE004	173	8.49	9.46	5.48	0.81	10.09	12.13	6.77	0.83

The root mean square (RMS) is given for each component of the compared data. The RMS difference (RMSD) and correlation coefficient (CC) are computed. N is the total number of data used for comparisons. RMS and RMSD are in cm/s

2.4 Encoding HFR data: empirical orthogonal functions

Empirical Orthogonal Functions (EOF) analysis of HFR velocities is a well-accepted method to determine the main modes of surface currents' variability (Sentchev and Yaremchuk 2007; Zhao et al. 2011; Cosoli et al. 2012, 2013; Kokkini et al. 2014). EOF decomposition is applied to the Cartesian velocity fields in order to extract the main variability patterns (Emery and Thomson 2001). Hourly, HFR velocity fields are decomposed in two separate space-time components (modes and amplitudes, respectively) as,

$$\mathbf{u}(x, y, t) - \langle \mathbf{u}(x, y, t) \rangle = \sum_{i=1}^{N_t} a_i(t) \text{EOF}_i(x, y) \quad (1)$$

where for each surface velocity at each time, the temporal average is removed, and the result is a combination of the EOF_i (mode) and a_i (amplitudes), for a $i = 1 : N_t$ mode number. The eigenvalues of the correlation matrix give the variance explained by their corresponding modes of variability. EOF is a projection of the original data in a new orthogonal base, hence, each mode can be interpreted in conjunction with the corresponding amplitude and validated by supplementary data. The original velocity fields can be recovered multiplying the modes EOF_i by their corresponding amplitudes a_i and summing up them following Eq. 1. A computationally efficient algorithm for the EOF decomposition is applied using the singular value decomposition (SVD) (Sayol et al. 2013). Only those nodes having more than an 85 % of data are included in a new data set which ends with a new grid having a coverage of 55 % of the original one. For each of the new grid, a continuous time series is created removing the temporal gaps. Eventually, SVD is applied over 9433 hourly data of (u, v) and EOF sorted in decreasing order according with their variance.

2.5 Wind-induced and total surface transport

We analyse the transport in the north-south direction across the section located at $38^\circ 49.46' \text{ N}$. The total surface transport is computed using HFR total velocities. The wind-induced transport is derived from Ekman velocities due to wind stress. For a steady and homogeneous ocean with friction, Ekman velocity components write (Stewart 2008):

$$(u, v) = V_0 \exp(\alpha z) [\cos(\pi/4 + \alpha z), \sin(\pi/4 + \alpha z)] \quad (2)$$

where $\alpha = \sqrt{f/2A_z}$ being f is the Coriolis parameter, A_z is the vertical diffusivity, and V_0 is the surface Ekman velocity. At the sea surface $z = 0$, currents have a speed V_0 and deflected $\pi/4$ to the right of the wind in the northern

hemisphere. The relation between V_0 and the wind speed at 10 m (U_{10}) can be readily obtained following (Ekman 1905) as,

$$V_0 = \frac{0.0127}{\sqrt{\sin|\varphi|}} \cdot U_{10} \quad (3)$$

where φ is the latitude.

Wind data at the IC mooring will be used hereinafter to compute the Ekman-transport. Wind homogeneity is assumed along the whole section to compute Ekman velocities. This hypothesis is supported by strong correlations ($CC \simeq 0.8$) between time series of zonal and meridional wind velocity components at the IC mooring and at the GALF station. However, note that in average, wind speed is attenuated near the coast for zonal and meridional components ($BIAS = -1 \text{ m/s}$ and $RMSD < 3 \text{ m/s}$) due to land effects. These effects are under the scope of this paper and will not be considered.

3 Results

3.1 Circulation patterns

The averaged surface current map (Fig. 6) is subtracted from the hourly HFR data to compute the EOF modes. The mean field shows a southwards flow at the west side of the channel where the bathymetry is larger and recirculating eastwards being totally reversed at shallow waters.

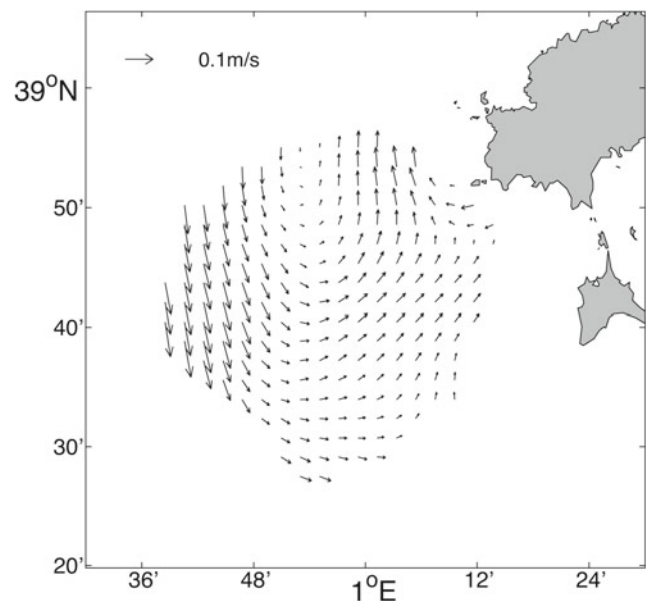


Fig. 6 Averaged HFR surface velocity for the period June 2012–January 2015

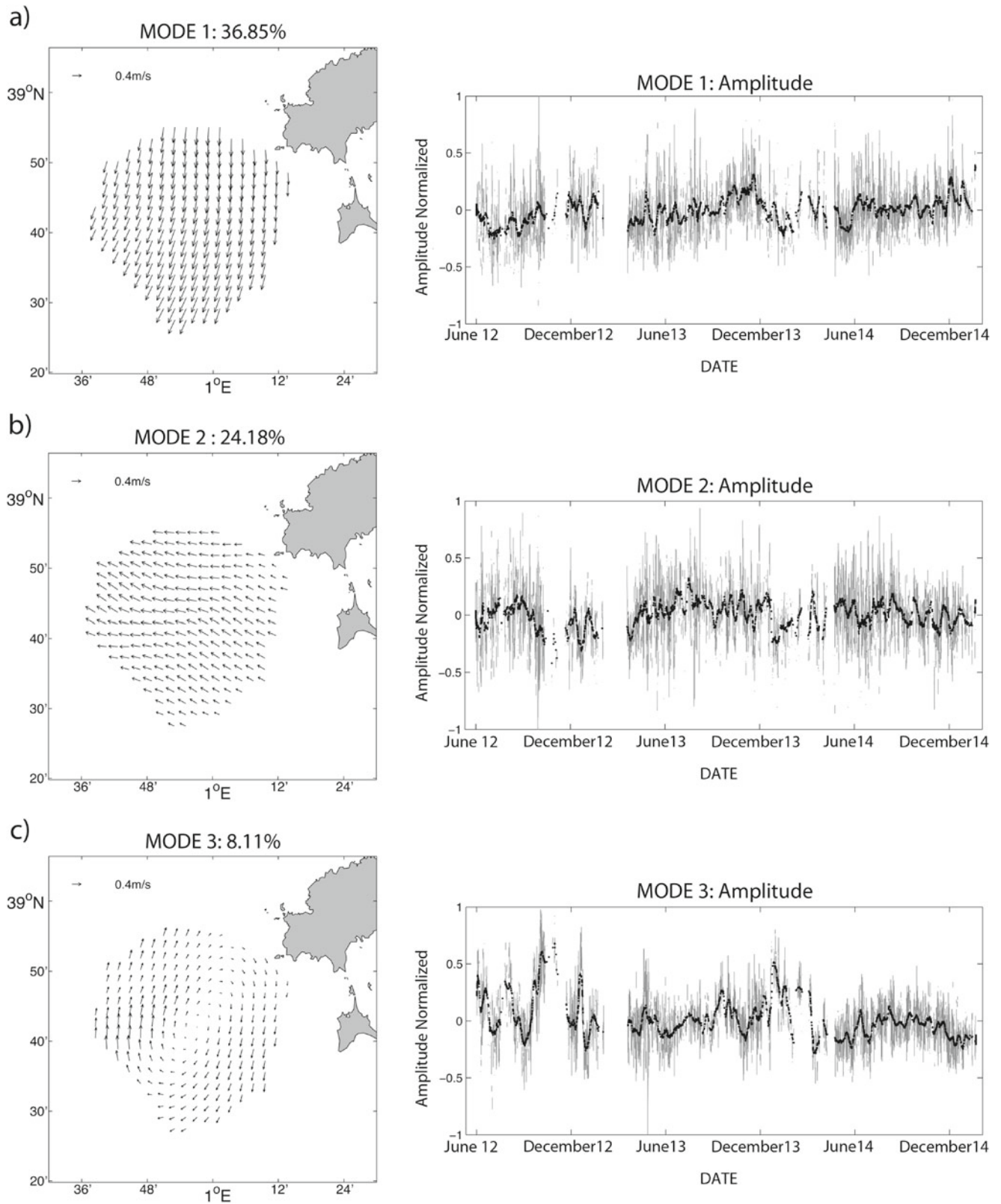


Fig. 7 EOF decomposition. **a** Mode 1 spatial pattern (*left*) and its associated normalized hourly (*black*) and 24-h smoothed (*gray*) temporal amplitude (*right*); **b** idem for Mode 2; **c** idem for Mode 3

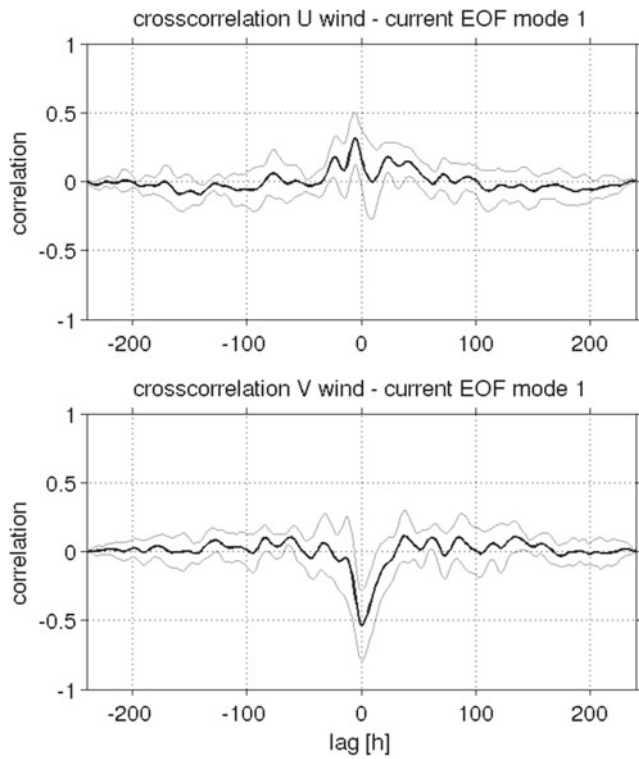


Fig. 8 Cross-correlation between zonal (*top*) and meridional (*bottom*) wind components and the temporal amplitude associated to the first mode of surface currents variability (*black curve*). Cross-correlation standard deviation deduced from block-averaging are added and removed to the cross-correlation (*grey line*). Lags are in hours

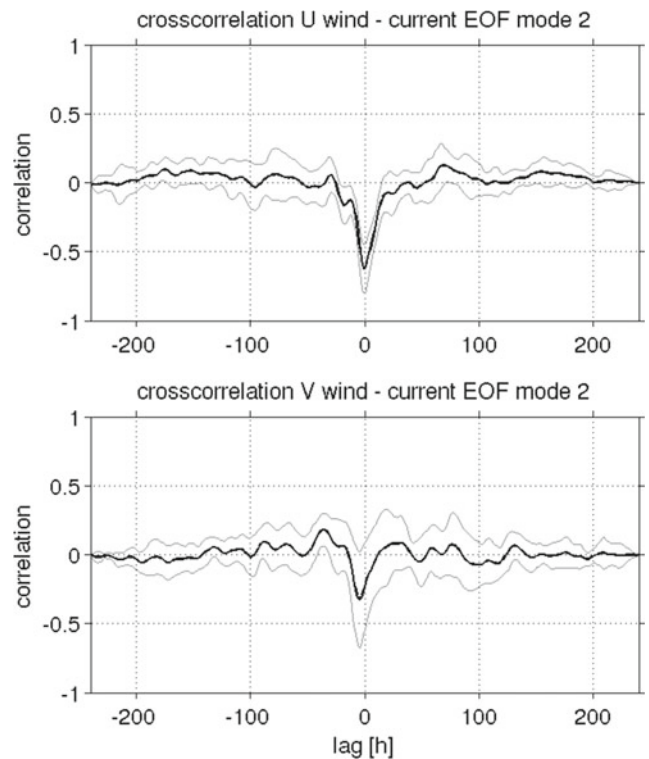


Fig. 9 Same as Fig. 8 for the second mode

The second mode explains 24 % of the total variance and represents an overall zonal flow. The amplitude shows

Usually in the EOF decomposition, the most statistically significant modes can be related with specific oceanic processes since they reflect the major part of the variance. Here, the first three EOFs explain 70 % of the total variance and the rest are the result of a single episode or just noise being difficult to interpret under a physical point of view. The modes are shown in Fig. 7, left panels, with their associated amplitudes, right panels. EOF have been normalized by the maximum of their temporal amplitudes in order to compare them. For sake of clarity, 7 days cut-off low-pass filtered temporal amplitudes have been superimposed.

The first mode which accounts for 37 % of the total variance represents an overall meridional flow. Positive (negative) values of the temporal amplitude during winter represent a southward (northwards) flow that, depending on the value of the amplitude, reflects stronger or weaker currents. During winter (NDJ), the amplitude of the first mode is mostly positive with large values at specific dates. In the Ibiza Channel, southwards flow has been already related with strong winds associated with storms moving towards south (Jansa 1987; Monserrat et al. 2008). Conversely, during summer (JJA), the amplitude is mainly negative and the resulting flow is directed northwards.

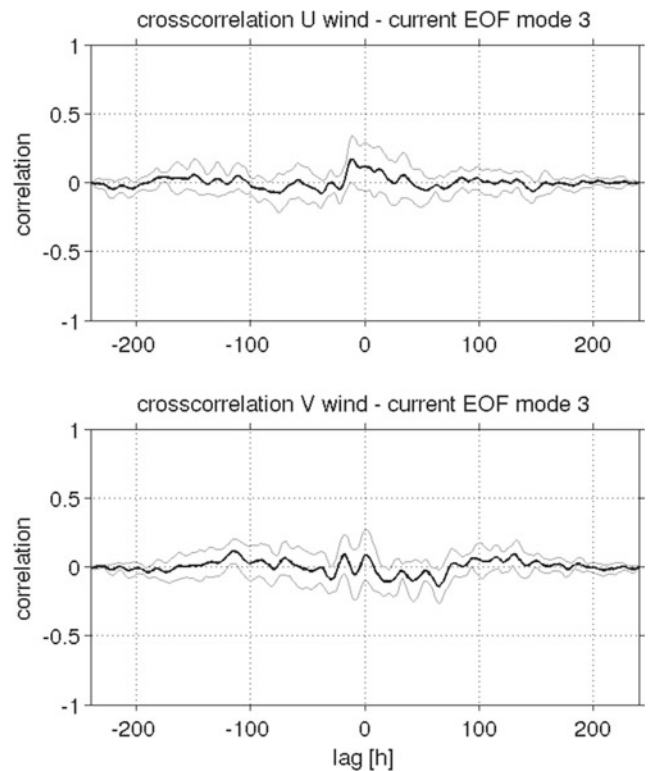


Fig. 10 Same as Fig. 8 for the third mode

a high temporal variability in this mode. A Fourier transform analysis gives spectral peaks ranging from 6 to 30 h and including inertial and tidal oscillations.

Finally, the third mode which explains 8 % of the total variability presents an eddy-like pattern, here too with high temporal variability. This structure has been recently identified as responsible of the blocking passage of rAW to the northern basin (Ruiz et al. 2009; Heslop et al. 2012). This mode is related to mesoscale circulation.

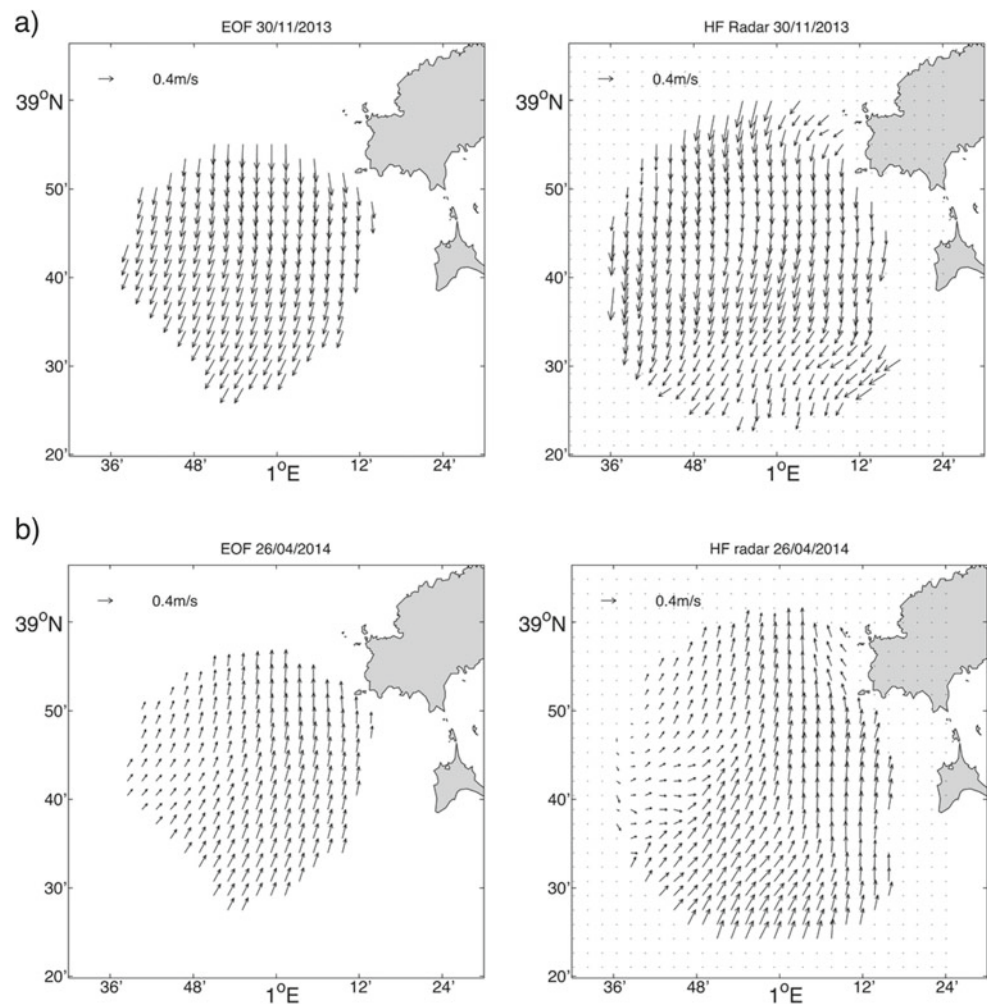
EOF₁ and EOF₂ reflect the response of the ocean surface to the dominant winds in the area (Fig. 4). To infer the relevance of local winds in driving these modes, cross-correlation between zonal and meridional wind components and the first three temporal amplitudes are computed (Sentchev and Yaremchuk 2007). Cross correlations are performed by block-averaging 10 days non-overlapped running windows. This length is chosen to ensure enough decorrelation between wind and current and to prevent spurious correlation induced by too long windows. Cross correlations between wind components and the first, second, and third mode are shown in Figs. 8, 9, and 10, respectively,

together with the standard deviations. The meridional wind component and the first temporal amplitude show the largest correlation (-0.54) (Fig. 8, bottom) at time lag 0 h. On the contrary, the zonal wind component and the first temporal amplitude cross correlation fails to pass the 99 % confidence level criterion (0.42 at time lag 0 h). It implies that northwards winds force the ocean surface currents to flow in the same direction with temporal scale less than half the temporal discretization of 1 h.

The correlation between the second amplitude and the zonal wind component is the largest (-0.63) (Fig. 9 top) at time lag 0 h. Besides the correlation between meridional wind component and the second amplitude are below the 99 % criterion (Fig. 9 bottom). It indicates again the instantaneous response of the ocean currents to this wind component in the same direction.

The amplitude of the third mode does not show any correlation with the wind (Fig. 10) indicating that the third mode represents other processes not directly induced by the wind forcing. The same analysis with higher order modes lead to the same result.

Fig. 11 Current field reconstructed with EOF modes (left) and HFR data snapshots (right) when mode 1 dominates over mode 2 for $a_1 > 0$ (a) and $a_1 < 0$ (b). In (a) $a_1 = 0.8$ and the wind velocity measured at the mooring station was $|u_{\text{wind}}| = 25.3$ m/s with an angle (oriented from the north and measured clockwise) of $\theta = 20^\circ$ (NNE). In (b), $a_1 = -0.5$ and the wind velocity measured at the buoy station was $|u_{\text{wind}}| = 8.4$ m/s, with an angle of $\theta = 203^\circ$ (SSW)



To further explore the wind influence in the first two EOF modes, we search from their temporal amplitudes the dates where one mode dominates over the other. We select two cases where the first mode dominates ($|a_1| \gg |a_2|$). In November 30th 2013 at 21 UTC ($a_1 > 0$) and the amplitude of the second mode is $a_2 \simeq 0$. Figure 11a, left panel, shows the reconstructed velocity for this date using only the first five EOFs. Note that this reconstructed field is similar to the first EOF mode (Fig. 7a, left). For the same date, the velocity field measured by the HFR is shown in Fig. 11a, right panel. As observed, the dynamics is mainly governed by the first mode being the result of strong winds blowing from north-south direction. This is a common situation since gale-force mistrals often develop when cyclogenesis occurs over the northern basin of the Mediterranean Sea all around the year but specially during end summer to winter (Estournel et al. 2003; Orfila et al. 2005; Canellas et al. 2007).

Although less frequent and less intense, there are also northward winds in the area. Figure 11b, left, shows the reconstructed surface velocity field for April 26th 2014

using 5 EOF when $a_1 < 0$ and $a_2 \simeq 0$. In this case, the surface velocity field is similar than the provided by EOF₁ weakened and reversed. The measured HFR velocity field is shown for the same instant in Fig. 11b, right. Note again that surface flow can be almost totally explained by EOF₁.

Regarding EOF₂, we identify dates where the second mode dominates ($|a_1| \gg |a_2|$). Figure 12a displays the reconstructed velocity field using the first five modes for August 13th 2014 at 22 UTC (left panel) when $a_2 > 0$. The total surface currents measured by the HFR are shown in Fig. 12a, right panel, where it can be observed the westwards main flow. Note that, even if the flow is deflected from the wind direction to the right at roughly 45°, it is difficult to link this result to the Ekman theory. Further investigations should be undertaken to better interpret this situation.

In April 4th 2014, the amplitude of the second mode is $a_2 < 0$. The reconstructed signal using the first five modes is displayed in Fig. 12b, left panel, together with the measured HFR velocities (right). As observed, the velocity field

Fig. 12 Current field reconstructed with EOF modes (left) and HFR data snapshots (right) when mode 2 dominates over mode 1 for $a_2 > 0$ (a) and $a_2 < 0$ (b). In (a), $a_2 = 0.8$ and the wind velocity measured was $|u_{wind}| = 13.2$ m/s with an angle of $\theta = 93^\circ$ (E). In (b), $a_2 = -0.7$ and the wind velocity $|u_{wind}| = 15.2$ m/s with an angle of $\theta = 283^\circ$ (W)

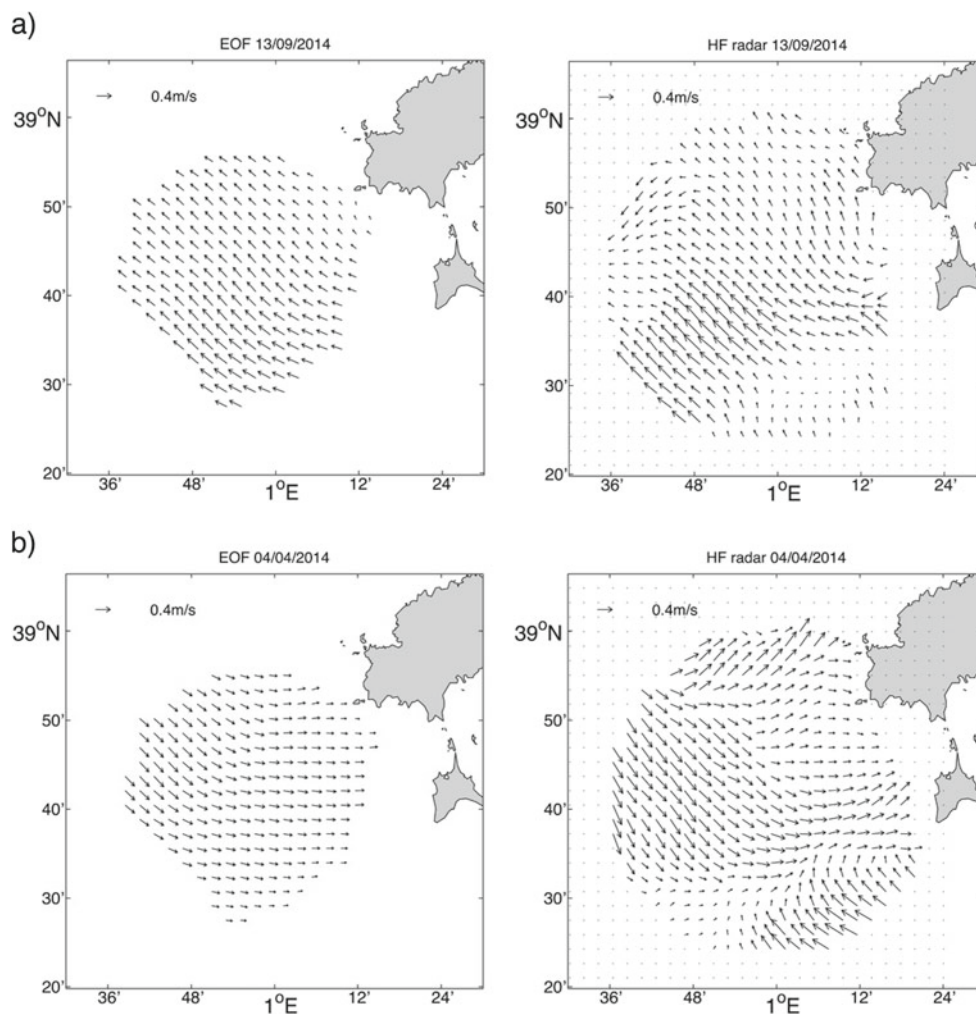


Table 3 Mean northernward and southerward transports calculated by the use of HFR and Ekman currents, for full and for summer (SUM) corresponding to July–August–September (JAS) and for winter (WIN)

corresponding to November–December–January (NDJ), for the first surface meter, and for a transect of 51 km in the Ibiza Channel

	Total	WIN 2014	SUM 2014	WIN 2015
HFR				
Northwards	0.004 (45 %)	0.004 (48 %)	0.003 (48 %)	0.003 (27 %)
Southwards	0.006 (55 %)	0.006 (52 %)	0.004 (52 %)	0.007 (73 %)
Ekman				
Northwards	0.002 (42 %)	0.001 (29 %)	0.003 (55 %)	0.002 (36 %)
Southwards	0.004 (46 %)	0.004 (62 %)	0.002 (16 %)	0.004 (60 %)

Transport in Sv ($10^6 \text{ m}^3/\text{s}$). Percentage of data involved for each direction is given between parenthesis. Periods with nule wind-induced transport are between 4 and 29 % of the time for WIN and SUM, respectively

can be inferred mostly from the second EOF representing the the surface flow induced by easterlies-westerlies.

The third EOF although associated with specific atmospheric events has a more complex explanation, and a coupled atmosphere-ocean model is needed to fully infer its dynamics.

3.2 Cross-channel mass transport

Cross channel transport is computed from HFR velocities along a transect at $38^\circ 49.46' \text{ N}$ coinciding with the mooring location. Transport is integrated for the first meter assuming that the velocity from the HFR is constant within this depth as well as the same each 3 km (resolution of the HFR). Besides, Ekman transport is computed using wind measurements at the buoy and applying Eq. 2.

The HFR and Ekman transports (in Sv) are summarized in Table 3 for the whole period. For completeness, Table 3 gives also the percentage of data involved for each direction (between parenthesis). There are calm periods –4 % in winter (JAS stating for July–August–September) and 29 % in summer (NDJ stating for November–December–January) of the time and then the transport is zero. In the Ibiza Channel, the HFR transport during winter is mainly southwards with a maximum averaged value during winter 2015 of 7×10^{-3} Sv occurring 73 % of time. During this season, the northwards transport from HFR is 3×10^{-3} Sv, 27 % of time. For the whole period, the southwards transport occurs 60 % of time with an averaged value of 6×10^{-3} Sv. The Ekman component of the transport is again mainly directed to the south with an averaged value during winter 2014 of 4×10^{-3} Sv 62 % of the record. Minimum transport is obtained during summer, as expected from the reduction of wind intensity in the area. In general, Ekman transport account between one-half and one-fourth of the total transport depending on the wind intensity.

4 Conclusions

Wind influence on the surface current variability is investigated using 2.5 years of continuous measurements of operational HFR velocities in the Ibiza Channel, an area that has been identified as a key geographical feature for the exchange of water masses. This study contributes to better understand the variability of the ocean dynamics and surface transport in this “chokepoint”. Nowadays, only HFR systems are able to provide high temporal and spatial resolutions and synoptic observations of surface currents in coastal environments.

To ensure the quality of operational velocities, a set of validation exercises have been performed. An Eulerian assessment of HFR was done by comparing the zonal and meridional velocity components of HFR with an ADCP and a CM moored in the area covered by the HFR. Besides, comparison of HFR currents is performed using surface drifters, a Lagrangian validation, that also provides an assessment of the spatial accuracy of the velocities measured by the HFR. This HFR system does not show significant bias, and its accuracy is in accordance with previous studies performed in other areas based on similar analysis.

The main circulation patterns are inferred from an EOF analysis. The first three modes represent almost 70 % of the total variability. A cross-correlation analysis between zonal and meridional wind components and the temporal amplitudes of the first three HFR EOF-modes are computed. Results from this analysis show that the surface current variability is mainly driven by local winds and can be explained mostly by two prevalent wind directions. EOF₁ which represents ~40 % of the total variability is the response of meridional winds while EOF₂ representing around ~20 % of the total variability is linked with zonal winds. Wind forcing have an immediate effects on the surface current generation. Third and higher modes are related to mesoscale

circulation features. In particular, the spatial distribution of the third mode is an eddy-like pattern, and it could be responsible of the blocking passage of rAW to the northern basin. Further studies are needed to better understand the importance of this structure.

Surface transport of water through the Ibiza Channel is significant. To evaluate and quantify the role of the wind-induced transport in the Ibiza Channel, the Ekman transport is compared against the total surface transport provided by the HFR velocities. We found that the Ekman transport in the Ibiza Channel is the most important component being on average around the 65 % of the total transport in the first meter. Transport present a markedly seasonal variability being mostly southwards. The intense transport of water masses during winter is highly reduced during summer months.

Estimation of mass transport at the ocean surface is of crucial importance from a scientific and societal point of view since many end users and applications require accurate measurements and predictions of dynamical properties at the surface boundary layer (e.g., from algae blooms, oils spill and SaR operations, larval connectivity, air ocean exchange among many others). The results from this work open the possibility of the development of new combined observing and forecasting systems combining HFR measurements with meteo-forecast in order to obtain short-term prediction of ocean surface currents. The analysis here presented is to be complemented by further works including 3D measurements based either on observations platforms such as gliders, altimetry data or ARGO floats, or on modeling and data assimilation in the context of coastal observing and forecasting systems.

Acknowledgments This work has been possible thanks to the collaboration between IMEDEA and SOCIB. Authors are indebted to the Marine Technologies and Operational Oceanography Department of IMEDEA and the Data Center and Engineering Facilities of SOCIB. A. Lana thanks the financial support from the CSIC-JAE doc program co-funded by the European Social Fund (ESF). J. Marmain is supported by Sur-Baleares Project. A. Orfila thanks the support from ENAP-Colombian Army through several grants. This work has been done thanks to the financial support from JERICO-NEXT project. Comments from Drs. J.M. Sayol, S. Ruiz, and P. Forget are greatly acknowledged.

Appendix

Statistical estimators used for comparisons are given here.

Let's define by $X_s(k)$, $k = 1, 2$, the two time series to be compared having a length N and being k the time index.

The root mean square (RMS) of the signal $X_s(k)$ is defined as

$$RMS_s = \sqrt{\frac{\sum_{k=1}^N X_s(k)^2}{N}} \tag{4}$$

The RMSD between $X_1(k)$ and $X_2(k)$ is defined as

$$RMSD = \sqrt{\frac{\sum_{k=1}^N (X_2(k) - X_1(k))^2}{N}} \tag{5}$$

The mean difference (BIAS) between $X_1(k)$ and $X_2(k)$ is defined as

$$BIAS = \frac{1}{N} \sum_{k=1}^N (X_2(k) - X_1(k)) \tag{6}$$

The correlation coefficient (CC) between $X_1(k)$ and $X_2(k)$ is defined as

$$CC = \frac{\text{cov}(X_1(k), X_2(k))}{\rho_{X_1} \rho_{X_2}} \tag{7}$$

where $\text{cov}(\cdot)$ is the covariance and ρ_{X_i} is the standard deviation of X_i .

References

- Barrick ED, Evans WM, Weber LB (1977) Ocean surface currents mapped by radar. *Science* 198(4313):138–144
- Bellomo L, Griffa A, Cosoli S, Falco P, Gerin R, Iermano I, Kalampokis A, Kokkini Z, Lana A, Magaldi MG, Mamoutos I, Mantovani C, Marmain J, Potiris E, Sayol JM, Barbin Y, Berta M, Borghini M, Bussani A, Corgnati L, Dagneaux Q, Gaggelli J, Guterman P, Mazzoldi A, Molcard A, Orfila A, Poulain PM, Quentin C, Tintore J, Uttieri M, Vetrano A, Zambianchi E, Zervakis V (2015) Toward an integrated hf radar network in the mediterranean sea to improve search and rescue and oil spill response: the TOSCA project experience. *J Oper Oceanogr* 8(2):95–107
- Canellas B, Orfila A, Mendez FJ, Menendez M, Gomez-Pujol L, Tintore J (2007) Application of a POT model to estimate the extreme significant wave height levels around the Balearic Sea (Western Mediterranean). *J Coast Res* 50:329–333
- Chapman RD, Shay LK, Graber HC, Edson JB, Karachintsev A, Trump CL, Ross DB (1997) On the accuracy of HF radar surface current measurements: intercomparisons with ship-based sensors. *J Geophys Res Oceans* 102(C8):18,737–18,748
- Cosoli S, Mazzoldi A, Gacic M (2010) Validation of surface current measurements in the Northern Adriatic Sea from High-Frequency Radars. *J Atmos Ocean Technol* 27(5):908–919
- Cosoli S, Bolzon G, Mazzoldi A (2012) A real-time and offline quality control methodology for seasonal high-frequency radar currents. *J Atmos Ocean Technol* 29(9):1313–1328
- Cosoli S, Ličer M, Vodopivec M, Malačič V (2013) Surface circulation in the gulf of trieste (northern adriatic sea) from radar, model, and adcp comparisons. *J Geophys Res Oceans* 118(11):6183–6200
- Crombie DD (1955) Doppler spectrum of sea echo at 13.56 Mc/s. *Nature* 175(4459):681–682

- Ekman VW (1905) On the influence of the Earth's rotation on ocean currents. *Arch Math Astron Phys* 2:1–52
- Emery WJ, Thomson RE (2001) Data analysis and methods in physical oceanography. Elsevier Science, Amsterdam
- Emery BM, Washburn L, Harlan JA (2004) Evaluating radial current measurements from CODAR high-frequency radars with moored current meters. *J Atmos Ocean Technol* 21(8):1259–1271
- Estournel C, de Madron XD, Marsaleix P, Auclair F, Julliand C, Vehil R (2003) Observation and modeling of the winter coastal oceanic circulation in the Gulf of Lion under wind conditions influenced by the continental orography (FETCH experiment). *J Geophys Res Oceans* 108(C3):8059
- Forget P (2015) Noise properties of hf radar measurement of ocean surface currents. *Radio Sci* 50(8):764–777
- Harlan J, Terrill E, Hazard L, Keen C, Barrick D, Whelan C, Howden S, Kohut J (2010) The integrated ocean observing system high-frequency radar network: status and local, regional, and national applications. *Mar Technol Soc J* 44(6):122–132
- Heslop EE, Ruiz S, Allen J, Luis Lopez-Jurado J, Renault L, Tintore J (2012) Autonomous underwater gliders monitoring variability at “choke points” in our ocean system: a case study in the Western Mediterranean Sea. *Geophys Res Lett* 39(20):1–6
- Jansa A (1987) Distribution of the mistral—a satellite observation. *Meteorol Atmos Phys* 36(1–4):201–214
- Juza M, Renault L, Ruiz S, Tintore J (2013) Origin and pathways of winter intermediate water in the northwestern mediterranean sea using observations and numerical simulation. *J Geophys Res Oceans* 118:6621–6633
- Kokkini Z, Potiris M, Kalampokis A, Zervakis V (2014) Hf radar observations of the dardanelles outflow current in the north eastern aegean using validated wera hf radar data. *Mediterranean Marine Science* 15(4):753–768
- Lana A, Fernandez V, Tintore J (2015) SOCIB continuous observations of ibiza channel using HF Radar technology for characterization and quantification of surface currents. *Sea Technol* 56(3):31–34
- Laws K (2001) Measurements of near surface ocean currents using HF radar. Master's thesis, Univ. of Calif., Santa Cruz
- Lipa BJ, Barrick DE (1983) Least-squares methods for the extraction of surface currents from CODAR crossed-loop data—application at Arsløe. *IEEE J Oceanic Eng* 8(4):226–253
- Liu YG, Weisberg RH, Vignudelli S, Mitchum GT (2014) Evaluation of altimetry-derived surface current products using lagrangian drifter trajectories in the eastern gulf of Mexico. *J Geophys Res Oceans* 119(5):2827–2842
- Lopez-Garcia MJ, Millot C, Font J, Garcia-Ladona E (1994) Surface circulation variability in the balearic basin. *J Geophys Res Oceans* 99(C2):3285–3296
- Lopez-Jurado JL, Lafuente JMG, Lucaya NC (1995) Hydrographic conditions of the Ibiza Channel during November 1990, March 1991 and July 1992. *Oceanol Acta* 18:235–243
- Lorente P, Soto-Navarro J, Alvarez Fanjul E, Piedracoba S (2014) Accuracy assessment of high frequency radar current measurements in the strait of gibraltar. *J Oper Oceanogr* 7(2):59–73
- Mason E, Pascual A (2013) Multiscale variability in the Balearic Sea: an altimetric perspective. *J Geophys Res Oceans* 118(6):3007–3025
- Millot C (1999) Circulation in the western mediterranean sea. *J Mar Syst* 20:423–442
- Monserrat S, Lopez-Jurado JL, Marcos M (2008) A mesoscale index to describe the regional circulation around the Balearic Islands. *J Mar Syst* 71(3–4):413–420
- Orfila A, Alvarez A, Tintore J, Jordi A, Basterretxea G (2005) Climate teleconnections at monthly time scales in the Ligurian Sea inferred from satellite data. *Prog Oceanogr* 66(2–4):157–170
- Orfila A, Molcard A, Sayol JM, Marmain J, Bellomo L, Quentin C, Barbin Y (2015) Empirical forecasting of HF-radar velocity using genetic algorithms. *IEEE Trans Geosci Remote Sens* 53(5):2875–2886
- Paduan JD, Rosenfeld LK (1996) Remotely sensed surface currents in monterey bay from shore-based HF radar (coastal ocean dynamics application radar). *J Geophys Res Oceans* 101:20669–20686
- Paduan JD, Washburn L (2013) High-frequency radar observations of ocean surface currents. *Ann Rev Mar Sci* 5(5):115–136
- Paduan JD, Kim KC, Cook MS, Chavez FP (2006) Calibration and validation of direction-finding high-frequency radar ocean surface current observations. *IEEE J Ocean Eng* 31(4):862–875
- Pinardi N, Allen I, Demirov E, De Mey P, Korres G, Lascaratos A, Le Traon PY, Maillard C, Manzella G, Tziavos C (2003) The Mediterranean Ocean Forecasting System: first phase of implementation (1998–2001). *Ann Geophys* 21(1):3–20
- Pinot JM, Ganachaud A (1999) The role of winter intermediate waters in the spring-summer circulation of the Balearic Sea—1. Hydrography and inverse box modeling. *J Geophys Res Oceans* 104:29843–29864
- Pinot JM, Tintore J, Gomis D (1994) Quasi-synoptic mesoscale variability in the Balearic Sea. *Deep-Sea Res I Oceanogr Res Pap* 41(5–6):897–914
- Pinot JM, Lopez-Jurado JL, Riera M (2002) The CANALES experiment (1996–1998). Interannual, seasonal, and mesoscale variability of the circulation in the Balearic Channels. *Prog Oceanogr* 55:335–370
- Renault L, Oguz T, Pascual A, Vizoso G, Tintore J (2012) Surface circulation in the Alboran Sea (Western Mediterranean) inferred from remotely sensed data. *J Geophys Res Oceans* 117(C08009):1–11
- Roarty H, Smith M, Kerfoot J, Kohut J, Glenn S (2012) Automated quality control of high frequency radar data 2012. *Oceans* (1):1–7
- Rubio A, Reverdin G, Fontan A, Gonzalez M, Mader J (2011) Mapping near-inertial variability in the SE Bay of Biscay from HF radar data and two offshore moored buoys. *Geophys Res Lett* 38:1–6
- Ruiz S, Pascual A, Garau B, Faugere Y, Alvarez A, Tintore J (2009) Mesoscale dynamics of the Balearic Front, integrating glider, ship and satellite data. *J Mar Syst* 78:S3–S16
- Sayol JM, Orfila A, Simarro G, Lopez C, Renault L, Galan A, Conti D (2013) Sea surface transport in the Western Mediterranean Sea: a Lagrangian perspective. *J Geophys Res Oceans* 118(12):6371–6384
- Sayol JM, Orfila A, Simarro G, Conti D, Renault L, Molcard A (2014) A Lagrangian model for tracking surface spills and SaR operations in the ocean. *Environ Model Softw* 52(0):74–82
- Schmidt RO (1986) Multiple emitter location and signal parameter estimation. *IEEE Trans Antennas Propag* 34(3):276–280
- Sentchev A, Yaremchuk M (2007) Vhf radar observations of surface currents off the northern opal coast in the eastern english channel. *Cont Shelf Res* 27(19):2449–2464
- Shay LK, Martinez-Pedraja J, Cook TM, Haus BK, Weisberg RH (2007) High-frequency radar mapping of surface currents using WERA. *J Atmos Ocean Technol* 24(3):484–503
- Solabarrieta L, Rubio A, Castanedo S, Medina R, Charria G, Hernandez C (2014) Surface water circulation patterns in the southeastern Bay of Biscay: new evidences from HF radar data. *Cont Shelf Res* 74:60–76
- Stewart RH (2008) Introduction to physical oceanography. Texas A&M University
- Stewart RH, Joy JW (1974) HF radio measurements of surface currents. *Deep-Sea Res* 21(12):1039–1049

- Tintore J, Vizoso G, Casas B, Heslop E, Pascual A, Orfila A, Ruiz S, Martinez-Ledesma M, Torner M, Cusi S, Diedrich A, Balaguer P, Gomez-Pujol L, Alvarez-Ellacuria A, Gomara S, Sebastian K, Lora S, Pau Beltran J, Renault L, Juza M, Alvarez D, March D, Garau B, Castilla C, Canellas T, Roque D, Lizaran I, Pitarch S, Antonia Carrasco M, Lana A, Mason E, Escudier R, Conti D, Manuel Sayol J, Barcelo B, Alemany F, Reglero P, Massuti E, Velez-Belchi P, Ruiz J, Oguz T, Gomez M, Alvarez E, Ansorena L, Manriquez M (2013) SOCIB: the Balearic Islands Coastal Ocean observing and forecasting system responding to science, technology and needs, society. *Mar Technol Soc J* 47(1):101–117
- Troupin C, Pascual A, Valladeau G, Pujol I, Lana A, Heslop E, Ruiz S, Torner M, Picot N, Tintore J (2015) Illustration of the emerging capabilities of SARAL/AltiKa in the coastal zone using a multi-platform approach. *Adv Space Res* 55(1):51–59
- Viudez A, Tintore J, Haney RL (1996) Circulation in the Alboran Sea as determined by quasi-synoptic hydrographic observations. I. Three-dimensional structure of the two anticyclonic gyres. *J Phys Oceanogr* 26(5):684–705
- Zavatarelli M, Mellor GL (1995) A numerical study of the Mediterranean-Sea circulation. *J Phys Oceanogr* 25(6):1384–1414
- Zhao J, Chen X, Hu W, Chen J, Guo M (2011) Dynamics of surface currents over qingdao coastal waters in august 2008. *J Geophys Res Oceans* 116(C10020):1–15